



Contents lists available at ScienceDirect

International Journal of Solids and Structures

journal homepage: www.elsevier.com/locate/ijsostr

Triaxial mechanical characterization of ultrasoft 3D support bath-based bioprinted tubular GelMA constructs

Ahsanul Torza¹, Ralf Zgeib¹, Xiaofeng Wang, Ahmadreza Zaeri, Fucheng Zhang, Kai Cao, Robert Chang, Johannes Weickenmeier*

Department of Mechanical Engineering, Stevens Institute of Technology, Hoboken, NJ 07030, United States of America

ARTICLE INFO

Keywords:

Support bath bioprinting
Tubular cell-laden GelMA constructs
Live-dead cell assay
Triaxial mechanical characterization
Inverse finite elements

ABSTRACT

Support bath-based extrusion bioprinting is an emerging additive manufacturing paradigm that allows for the creation of geometrically complex three-dimensional tissue-mimicking constructs. Although this approach enables arbitrary geometries to be printed, preserving shape and mechanical integrity after the construct is extracted from the support bath is one of the main challenges today. In the present study, we systematically tested the effect of critical printing parameters on construct integrity and stiffness. Specifically, we varied the concentration and temperature of the bioink and support bath material, hydrogel crosslinking time, and cell density of the bioink. While previous studies on hydrogel materials quantify construct properties based on a single loading mode—such as uniaxial testing or rheological experiments, for example—we used a multiaxial mechanical testing protocol to assess the printed construct's response in tension, compression, and shear. For each sample, we determined a single set of material parameters by simultaneously fitting all three modes in our inverse finite element framework. In support of future modeling work, we analyzed three different constitutive models with respect to their ability to match the construct's mechanical response. We observed that GelMA concentration, temperature, and cell density have a statistically significant effect on the construct stiffness; support bath temperature and UV crosslinking time have a weak effect on construct stiffness; and support bath concentration appears to have no direct effect on the measured construct properties. Our construct stiffness were found to vary between 0.07 and 2.2 kPa depending on printing conditions, and showed noticeable tension–compression asymmetry as well as pronounced nonlinear behavior when loaded under shear.

1. Introduction

Bioprinting, a rapidly evolving technique in tissue engineering and regenerative medicine, and a critical capability of additive manufacturing for various biological applications, has significantly advanced the fabrication of complex three-dimensional structures (Mandrycky et al., 2016). This technology has emerged as an enabling approach for precision fabrication of printed constructs that mimic human tissues' native architecture and functionality (Melchels et al., 2012; Harding et al., 2023). Among the various bioprinting techniques, support bath printing and in-air printing are particularly noteworthy. Traditional in-air printing involves stacking material upon itself, relying on the stability, mechanical strength, and interlayer connectivity of previous layers (Ahmadi Soufivand et al., 2023). This printing paradigm is limited with respect to the printability of bioinks with low viscosities. Support bath printing, on the other hand, features the ability to print

large, structurally complex constructs without additional support structures (McCormack et al., 2020). It operates by extruding bioink into a support bath material with thixotropic properties, capable of self-suspending the bioink, and after *in situ* crosslinking, forms cohesive 3D constructs ready for extraction from the support bath (Ding and Chang, 2018). This bioprinting technique enables the fabrication of tissue constructs with low viscosity hydrogels, promoting better cellular viability and function.

Gelatin methacryloyl (GelMA) is a widely used bioink in bioprinting due to its excellent biocompatibility, tunable mechanical properties, and ability to support cell adhesion, proliferation, and differentiation (Piao et al., 2021). The bioprinting process involves the extrusion of bioink through a nozzle to create three-dimensional structures layer by layer. GelMA is particularly favored for its photocrosslinkable properties, which allow for rapid and precise solidification under UV light, thus maintaining the structural integrity of the printed constructs (Yue

* Corresponding author.

E-mail address: johannes.weickenmeier@stevens.edu (J. Weickenmeier).

¹ These two authors contributed equally to this work.

<https://doi.org/10.1016/j.ijsostr.2024.112938>

Received 12 March 2024; Received in revised form 16 June 2024; Accepted 18 June 2024

Available online 22 June 2024

0020-7683/© 2024 Elsevier Ltd. All rights reserved, including those for text and data mining, AI training, and similar technologies.

et al., 2015). Moreover, the mechanical properties of GelMA can be finely tuned by varying the degree of methacrylation and the concentration of gelatin, enabling the fabrication of constructs with tailored stiffness and elasticity suitable for different tissue engineering applications (Yue et al., 2015). This adaptability is crucial for mimicking the diverse mechanical environments of native tissues, from soft tissues like liver and brain to more rigid structures like cartilage and bone (Tripathi et al., 2023; Bessot et al., 2023).

The mechanical properties of bioprinted constructs are critical for their functionality and compatibility with host tissue, as highlighted by Mironov et al. (2003). For example, Pahoff et al. (2019) reported on the effect of material parameters including GelMA concentration and the degree of methacrylation on the mechanical properties of GelMA-based cartilage constructs. Moreover, Klotz et al. (2016) demonstrated that incorporating endothelial cells and human mesenchymal stem cells into a GelMA bioink enhances both the mechanical properties and vascularization of bioprinted liver tissue constructs. Additionally, computational models have been developed to predict the mechanical behavior of bioprinted constructs based on material properties and printing parameters (Poldervaart et al., 2014; Jin et al., 2022). Despite recent advancements in support bath printing, challenges remain, particularly in the precise control of the mechanical properties and post-processing of the bioprinted constructs. This impedes the effective production of softer tissues and organs, such as heart tissue (Roche et al., 2021), blood vessels (Xu et al., 2020), skin (Xu et al., 2023), and brain tissue (Tang et al., 2021). This limitation necessitates a comprehensive investigation into key printing parameters of the bioink and support bath materials that enhance the mechanical properties while preserving cell viability of the final constructs (Brunel et al., 2022; Navara et al., 2023).

The objective of the present work is to understand the effects of fabrication parameters on the mechanical properties of support-bath printed constructs made of (cell-laden) photocrosslinkable hydrogel bioink gelatin methacryloyl, or GelMA. We use GelMA for its tunable mechanical properties and compatibility with cell-adhesive peptides which enhance cell growth, differentiation, and proliferation (Yin et al., 2018; Zhu et al., 2016). Support bath printing of low-concentration, low-viscosity GelMA enables us to selectively deposit cell-laden materials layer by layer to construct desired geometries, thus showing promise for complex soft tissue and other similar applications (Zgeib et al., 2023a). Specifically, we create hollow cylindrical structures that mimic vasculature in order to understand the effect of six key printing parameters on construct stiffness: the concentration and temperature of the bioink and support bath material, UV crosslinking time, and cell density of the bioink. We prepare three samples for each set of printing parameters and perform measurements with our custom-built triaxial testing device. Specifically, we examine GelMA under three loading modes: tension, compression, and shear. We use an inverse finite element approach to determine model parameters (for the Neo-Hookean, Ogden, and Gent model) that best fit all three loading modes simultaneously. Lastly, we perform a cell viability study to assess cell survival in our low-concentration tubular constructs across a 7-day observation period.

2. Methods

2.1. Bioink and support bath material preparation

GelMA material was prepared following a protocol presented by Ding et al. (2019). To that end, lithium phenyl-2,4,6-trimethylbenzoyl phosphinate (LAP) (Allevi by 3D Systems, PA, USA) was fully dissolved in Dulbecco's Phosphate Buffered Saline (DPBS) (R&D Systems, MN, USA) at 60 °C for 30 min with 0.5% w/v concentration of the final solution. The solution was stored in a light-protected container to prevent premature photoinitiator activation from exposure to light. When LAP was fully dissolved in DPBS, lyophilized GelMA foam (Allevi

by 3D Systems, PA, USA) was added to the solution with a 10% w/v final concentration and mixed at 60 °C for at least one hour in the dark. The GelMA batch was then stored at 4 °C for no more than 7 days before use.

Support bath material was prepared following the protocol presented by Ding and Chang (2018). First, powder Laponite B (BYK Additives Inc., Gonzales, USA) was autoclaved using dry settings at 120 °C. Next, appropriate amounts of sterile Laponite B were slowly and continuously dissolved in deionized distilled water (1.0, 1.5, and 2% w/v) while being stirred at 30 °C for 1 h until full dispersion and homogenization was reached. Finally, the solution was cooled to room temperature and stored in a closed container at 4 °C.

Prior to sample preparation:

- To prepare sterile GelMA inks *without* cells, we melted GelMA in a warm water bath at 37 °C, poured it into a 3 mL syringe that was covered with aluminum foil to prevent photocatalysis of GelMA, i.e., undesired crosslinking, and mounted it in the custom-made quad-extrusion bioprinting system.
- To prepare sterile GelMA inks *with* cells, i.e., *bioinks*, we melted GelMA in a warm water bath at 37 °C and then filtered it using a 0.22 μm vacuum filter cup under aseptic conditions. The vacuum filter was first wetted with DPBS to allow easier flow of GelMA without significant loss in total volume. Cells were collected as a pellet after centrifuging the cells at 350 RPM for 3 min. The cell pellet was mixed with cell media before we pipetted GelMA until a final concentration of 5% w/v cell-laden GelMA bioink was reached. The final cell density was approximately 1.5×10^6 cells/mL.

2.2. Support bath-based bioprinting of GelMA

To mimic arterial tissue, we used a hollow cylinder sample geometry with outer diameter $D=7$ mm, inner diameter $d=3$ mm, and height $H=7$ mm. We used a custom-made quad-extrusion bioprinting system to bioprint samples with GelMA bioinks, see Fig. 1a (Zgeib et al., 2023a,b). We used Cura (Cura Ultimake, Zaltbommel, NL) to obtain an initial toolpath g-code from the sample's CAD model which we modified to meet the requirements of our quad-extrusion bioprinting system. The prepared GelMA bioink was loaded into a 3 mL sterile syringe equipped with a 1.25" 22G nozzle (Nordson EFD, RI, USA) and wrapped in aluminum foil to prevent photocatalysis of GelMA, i.e., in this case premature crosslinking. The syringe was then heated to the prescribed printing temperature, and mounted on the quad-extrusion bioprinting system for printing.

During in-air printing, 3 hollow cylinders were printed side-by-side on a glass slide. In the case of support bath-based printing, we filled a 15 mL glass Pyrex beaker with the support bath material and printed 3 vertically-staked cylinders in one session. In Fig. 1b, we show the printing of a single GelMA cylinder. The printed structures were crosslinked with an 8 W, 365 nm ultraviolet light (UVP, UVL-18 365 nm UV light, Analytik Jena US, CA, USA) for 40 s to 60 s depending on the prescribed printing protocol. The cylinders were then removed from the support bath, rinsed with DPBS, and cleaned from excess liquids using a KimWipe. The last step ensured full adhesion when mounting the sample in the triaxial testing machine, on the one hand, and prevented sample swelling during mechanical testing, on the other.

2.3. Printing parameters considered in this study

We quantified the effect of 6 bioprinting process parameters on sample stiffness. Specifically, we evaluated the effect of three different support bath temperatures (4 °C, 24 °C, and 37 °C), three different LaponiteB concentrations (1%w/v, 1.5%w/v, and 2%w/v), two different GelMA temperatures (24 °C and 37 °C), three different GelMA concentrations (5%w/v, 7%w/v, and 10%w/v), three different UV crosslinking times (40s, 50 s, and 60s), and four different cell density (0, 1.5, 3, and 6 million cells/mL) as summarized in Table 1. Our

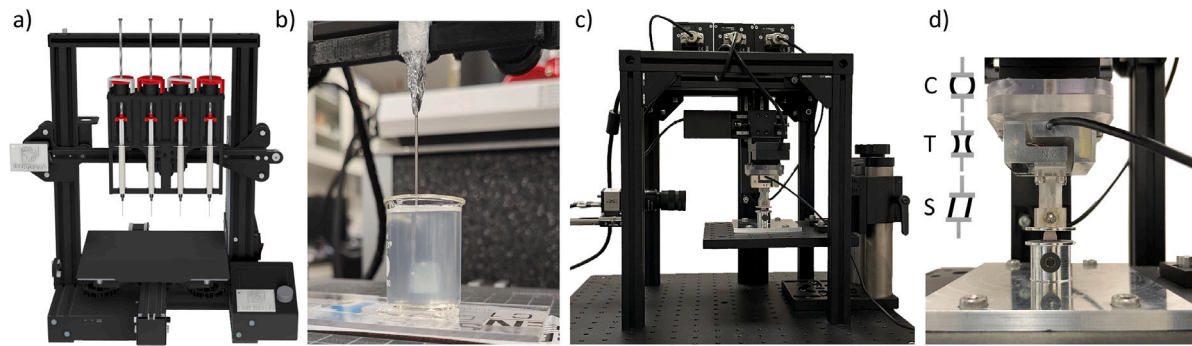


Fig. 1. Setup of (a) the custom-made quad-extrusion bioprinting machine and (b) a representative image of GelMA being deposited in the LaponiteB-based support bath. Setup of (c) the custom-made triaxial testing device and (d) a close-up view of a GelMA cylinder placed inside the testing device prior to experimentation. Additionally, 2D schematics are included to demonstrate the compression (C), tension (T), and shear (S) experiments performed on the GelMA constructs.

Table 1

Support bath (SB) and in-air printing parameters evaluated for their impact on sample stiffness. Default printing parameters are 24 °C support bath (SB) temperature, 1.5%w/v LaponiteB (LapB) concentration, 24 °C gelatin methacryloyl (GelMA), 5%w/v GelMA concentration, and 40 s crosslinking (CL) time. We refer to ink or bioink depending on the presence of cells (group 6). In air printing parameters were selected based on previous work (Ding and Chang, 2018; Ding et al., 2019). Numbers highlighted in red show the specific values selected for the individual printing parameter that was varied in our 7 different groups.

group #	SB temp [°C]	LapB concentr [%w/v]	GelMA temp [°C]	GelMA concentr [%w/v]	CL time [seconds]	cell density [mcells/mL]
SUPPORT BATH PRINTED SAMPLES						
1	4	1.5	24	5	40	0
1	24	1.5	24	5	40	0
1	37	1.5	24	5	40	0
2	24	1	24	5	40	0
2	24	1.5	24	5	40	0
2	24	2	24	5	40	0
3	24	1.5	24	5	40	0
3	24	1.5	37	5	40	0
4	24	1.5	24	5	40	0
4	24	1.5	24	7	40	0
4	24	1.5	24	10	40	0
5	24	1.5	24	5	40	0
5	24	1.5	24	5	50	0
5	24	1.5	24	5	60	0
6	24	1.5	24	5	40	0
6	24	1.5	24	5	40	1.5
6	24	1.5	24	5	40	3
6	24	1.5	24	5	40	6
IN AIR PRINTED SAMPLES						
7	N/A	N/A	21	7	40	0

default printing parameters were: 24 °C support bath and bioink temperature, a 1.5%w/v support bath and 5%w/v bioink concentration, respectively, 40 s UV crosslinking time, and no cells because these parameters provide the necessary stiffness for a stable yet compliant soft structure based on previous work (Ding et al., 2019; Ding and Chang, 2018). The cell-laden constructs were tested immediately after printing. Specifically, after their culturing, cells were harvested as a pellet and mixed with GelMA. Once printed into the support bath, the constructs were immediately extracted, washed with PBS to remove excess support batch medium, and lightly dried with a Kim Wipe before mechanical testing.

We also prepared in-air printed samples for comparison against support bath printed samples and used a GelMA temperature of 21 °C, GelMA concentration of 7%w/v, and 40 s UV crosslinking time. The parameters for in air printing were based on previous work and provide among the softest possible samples that maintain shape and do not collapse under their own weight (Ding et al., 2019; Ding and Chang, 2018).

Justification for select printing parameters: Printing parameter settings were determined based on values reported in literature, device specifications, and observed limitations to our construct's integrity.

Specifically, GelMA concentrations of 5%w/v, 7%w/v, and 10%w/v are widely used in literature; UV crosslinking times of 40 s, 50 s, and 60 s strike a balance between ensuring structural integrity and supporting cellular activity and survival (Ding et al., 2019; Xu et al., 2022); lack of active temperature control of our printing device limits us to few possible temperature settings: 24 °C, i.e., room temperature, as a default bioink and support bath material temperature; 37 °C to simulate physiological conditions by pre-heating both materials prior to printing; and 4 °C for the support bath material by cooling in an ice bath prior to printing (Li et al., 2022). We cannot print GelMA bioinks below 20 °C due to their thermal gelation (Mancha Sánchez et al., 2020). The concentration of the support bath material, Laponite B, was varied between 1%w/v, 1.5%w/v, and 2%w/v, based on the manufacturer's guidelines and the lack of existing characterizations (Shafran et al., 2020). The manufacturer suggests a maximum concentration of 2%w/v to maintain optimal thixotropic behavior. Accordingly, we selected concentrations of 1%w/v, 1.5%w/v, and 2%w/v for our study, with 1.5%w/v serving as the standard concentration for our experimental groups. Both cell type and cell density in the bioink play a crucial role in influencing the mechanical properties of bioprinted constructs (Krishnamoorthy et al., 2019).

2.4. Multi-axial mechanical testing of GelMA samples

We tested the multiaxial construct response using a custom-built tri-axial testing machine based on the designs of [Sugerman et al. \(2021\)](#) and [Kakaletsis et al. \(2021\)](#). Figs. 1c/d show the system configuration with three linear stages (Thorlabs, NJ, USA) in tandem with a three-axis 2N force sensor (Interface, AZ, USA). We glued each sample between two concentrically aligned pins with cyanoacrylate glue (The Gorilla Glue Company, OH, USA) and used two orthogonal cameras to measure the sample's overall dimensions required for the conversion of forces and displacements to stress and strain. Each sample underwent the following loading protocol: we prescribed 3 loading cycles up to 10% compressive strain, then 10% tensile strain, and lastly -20 to $+20\%$ shear strain at a constant displacement rate of 0.03 mm/s. After mechanical testing was completed, we converted the force–displacement data to stress–strain data. More specifically, we report the first Piola–Kirchhoff stress and nominal strain. We then isolated the third loading cycle with the intent to discard any preconditioning effects during the previous two cycles. Moreover, we ignored the material's viscous response and averaged the stress–strain curve's upstroke and downstroke. This provided us with the sample's 'elastic' response which we subsequently used for hyperelastic constitutive model parameter identification ([Budday et al., 2017](#); [Sugerman et al., 2021](#)). We consider our applied strain levels to be reasonably similar to in vivo strains of arteries. During normal function, arteries undergo cyclic deformations due to pulsatile blood flow, resulting in circumferential strains ranging from about 2–20% ([Lin et al., 2008](#); [Morrison et al., 2009](#)), while axial strains along the artery are observed to be on the order of a few percent ([Larsson et al.](#)). Moreover, our proposed strain levels are similar to what is applied in many ex vivo studies aiming at quantifying the mechanical properties of real arterial tissue using various testing setups ([Camasão and Mantovani, 2021](#)).

2.5. Hyperelastic model parameter identification

Hyperelastic models have been widely used to describe the mechanical behavior of GelMA ([Castilho et al., 2018](#); [Li et al., 2016](#); [Teixeira and Martins, 2023](#); [Narayanan et al., 2019](#); [Banerjee et al., 2021](#)). Here, we aim to identify the strain energy density function that best represents our GelMA data and, in turn, determined the model parameters of the Neo-Hookean, one-term Ogden, and Gent model.

To characterize finite deformations, we introduce the transformation Φ that maps material particles \mathbf{X} from the undeformed configuration to particles, $\mathbf{x} = \Phi(\mathbf{X})$, in the deformed configuration. Relative deformations within the sample are then given by the deformation gradient \mathbf{F} , i.e., the gradient of the deformation map Φ with respect to the undeformed coordinates \mathbf{X} , and its Jacobian J ,

$$\mathbf{F} = \nabla_{\mathbf{X}}\Phi, \quad \text{with} \quad J = \det(\mathbf{F}) > 0. \quad (1)$$

To best capture the quasi-incompressible behavior of GelMA, the deformation gradient is multiplicatively split into the volumetric (spherical) \mathbf{F}_{vol} and isochoric (unimodular) $\bar{\mathbf{F}}$ part such that

$$\mathbf{F} = \bar{\mathbf{F}} \cdot \mathbf{F}_{vol}, \quad \text{with} \quad \mathbf{F}_{vol} := J^{1/3} \mathbf{1} \quad \text{and} \quad \bar{\mathbf{F}} := J^{-1/3} \mathbf{F}. \quad (2)$$

The models evaluated here are functions of the unimodular first principal invariant \bar{I}_1 , with $\bar{I}_1 = \bar{\mathbf{F}}^T : \bar{\mathbf{F}}$, or the unimodular principal stretches $\bar{\lambda}_i$, given by $\det(\bar{\mathbf{F}}) = \bar{\lambda}_1 \bar{\lambda}_2 \bar{\lambda}_3 = 1$. This approach warrants an additive split of the strain energy function into a deviatoric (deformational) and a dilatational (volumetric) part.

Neo-Hookean model. The neo-Hookean model is the simplest of all models and is defined by the free energy function that is constant in the first principal invariant, $(\bar{I}_1 - 3)$, scaled by the shear modulus, μ , in addition to a volumetric part, scaled by the bulk modulus κ ,

$$\psi^{\text{Neo-Hookean}} = \frac{1}{2} \mu (\bar{I}_1 - 3) + \frac{1}{2} \kappa (J - 1)^2. \quad (3)$$

Ogden model. The free energy function of the one-term Ogden model is expressed in terms of the principal stretches, $\bar{\lambda}_i$, and has three model parameters, shear modulus μ , nonlinearity parameter α , and bulk modulus κ ,

$$\psi^{\text{Ogden}} = \frac{2\mu}{\alpha^2} (\bar{\lambda}_1^\alpha + \bar{\lambda}_2^\alpha + \bar{\lambda}_3^\alpha - 3) + \frac{1}{2} \kappa (J - 1)^2. \quad (4)$$

Gent model. The Gent model is a phenomenological model initially developed for rubber elasticity ([Gent, 1996](#)) and was chosen here for its ability to capture a wide spectrum of strain-stiffening material behavior representative of soft biological materials ([Giolando et al., 2023](#)). The strain energy uses a linear logarithm of the first invariant, $(\bar{I}_1 - 3)$, and requires two parameters, i.e., shear modulus μ and a stiffening parameter for the first invariant J_m ,

$$\psi^{\text{Gent}} = -\frac{\mu J_m}{2} \ln \left(1 - \frac{\bar{I}_1 - 3}{J_m} \right) + \frac{1}{2} \kappa (J - 1)^2. \quad (5)$$

We used an inverse finite element approach to determine the model parameters that best approximate the combined material behavior observed in tension, compression, and shear experiments of the differently printed samples, respectively. We used FEBio for all simulations ([Maas et al., 2012](#)) and created a finite element mesh representative of our sample geometry, i.e., a hollow cylinder with outer radius 3.5 mm, inner radius 1.5 mm, and height 7 mm. We used a uniform seeding size of $1 \times 1 \times 1$ which resulted in a nonuniform element size of $0.75 \times 0.55 \times 1.00$ mm, and adding up to a total of 1400 linear hexahedral fully integrated C3D8 eight-node brick elements. To that end, we fixed all nodes on the bottom layer of the mesh to mimic gluing the sample to the test bed while prescribing displacement boundary conditions to the top layer to reproduce the three loading conditions. We minimized the total relative squared error (RSE), i.e., the difference between numerically predicted and experimentally observed construct response, using the Truncated Newton Conjugate-Gradient method and identified the model parameters for each of the three constitutive models. To that end, we implemented our optimization code in python 3.11.4. From the SciPy library, we used the `scipy.optimize.minimize` function to run the Truncated Newton CG optimizer. For our objective function, we defined the error as

$$RSE = \left[\sum_{i=1}^{n_t} \left(1 - \frac{P_i^{\text{sim}}}{P_i^{\text{exp}}} \right)^2 \right]_{\text{tension}} + \left[\sum_{i=1}^{n_c} \left(1 - \frac{P_i^{\text{sim}}}{P_i^{\text{exp}}} \right)^2 \right]_{\text{compression}} + \left[\sum_{i=1}^{n_s} \left(1 - \frac{P_i^{\text{sim}}}{P_i^{\text{exp}}} \right)^2 \right]_{\text{shear}}, \quad (6)$$

where P^{sim} and P^{exp} are the simulation-based and experimentally observed tensile, compressive, and shear stresses, respectively. We sample experimental and simulation stresses at strain intervals of 0.005 [-] for compression and tension measurements and 0.01 [-] for shear measurements to ensure that the total RSE weights uniaxial and shear loading conditions equally. Therefore, $n_t=20$, $n_c=20$, and $n_s=40$, are the number of data points from the tensile, compressive, and shear experiments, respectively. We assume GelMA to be nearly-incompressible and prescribe a Poisson's ratio of $\nu = 0.495$ following the example of previous works ([Miri et al., 2018](#); [Ansari et al., 2017](#)). We lean on the relation between elastic properties in linearly elastic materials during the optimization to prescribe the bulk modulus κ based on Poisson's ratio ν and each iteration's current shear modulus μ ,

$$\kappa = \frac{2\mu(1 + \nu)}{3(1 - 2\nu)}, \quad (7)$$

which yields a bulk-to-shear-modulus ratio of 100. Since this is rather low, i.e., a ratio of 1000 or $\nu = 0.4995$ enforces near-incompressibility much stronger, we performed a sensitivity analysis on our model and observed that volume changes are less than 1% across all elements.

We used the optimization framework to determine the shear modulus μ , nonlinearity parameter α , and the stiffening parameter for the first invariant J_m of our respective models and report mean model parameters for each printing configuration. Statistical analysis was carried out including each sample's specific model parameters.

2.6. Cell culturing and viability assay

Cell viability was assessed by creating 12 additional support bath printed samples inoculated with cells according to a protocol presented by Zhu et al. (2017). Specifically, we cultured endothelial cells from the human umbilical vein cell line EA.hy926 (ATCC, VA, USA) in Dulbecco's Modified Eagle Medium/Nutrient Mixture F-12 (DMEM/F-12) media containing 10% fetal bovine serum and 1% penicillin-streptomycin solution stored at 37 °C in a humidified 5% CO₂ incubator. Our cells were cultured in T75 flasks where they attached to the bottom of the flask as they proliferated. At passage 14 of culturing, cells were detached from the bottom of the flask using Trypsin. The cell media containing the floating cells was then transferred to a tube and centrifuged at 350 RPM for 3 min. This process separated the cells from the cell media and Trypsin. The cells, now present as a pellet at the bottom of the tube, were then either immediately mixed into the bioink for bioprinting. These cell-laden samples were either used for mechanical testing or stored at 37 °C in a humidified 5% CO₂ incubator for up to 7 days as part of our cell viability study. For latter, at 3, 5, and 7 days, 3 samples were prepared for live-dead staining respectively. We used the commercially available LIVE/DEAD™ Viability/Cytotoxicity Kit (Invitrogen, MA, USA). Tissue constructs were washed with DPBS and stained with 2 μ M Calcein blue AM (green live cell stain) and 4 μ M ethidium homodimer-1 (red dead cell stain) solution and then incubated for 45-60 min. This ensured full penetration of the stains to all cells inside the printed GelMA samples. After incubation, the stained constructs were washed with DPBS and imaged using the wide-field fluorescence microscope IX83P1ZX (Olympus, Tokyo, JP) with the Fluorescein-5-isothiocyanate (FITC) and tetramethylrhodamine (TRITC) channel filters such live cells appear green and dead cells appear red, respectively. Cell viability was ultimately defined as the ratio between number of live cells and total number of cells.

2.7. Statistical analysis

We plot the averaged stress-strain response from the third loading cycle of each loading condition to visualize the impact of printing parameters under tension, compression, and shear. We report the results from our material parameter identification in the form of mean and standard deviation of the model parameters for each set of printing parameters. To that end, we evaluated the differences between model parameters using GraphPad Prism (Dotmatics, MA, USA). Specifically, we included each individual measurement and selected two-way ANOVA with repeated measures and the Tukey-Kramer post-hoc test to determine statistical significance and indicate a significance level of $p < 0.05$ with *, $p < 0.01$ with **, $p < 0.001$ with ***, and $p < 0.0001$ with ****. Lastly, we assessed the impact of select printing parameters on cell viability across a 7 day observation period by reporting mean and standard deviation of cell counts.

3. Results

3.1. Mechanical response of support bath printed bioink

Fig. 2 shows the stress-strain curves of groups 1 through 6. We averaged the data from all three samples per printing configuration and show mean and standard deviation for comparison between groups. The left column shows stress-strain curves for compression and tension, the right column shows stress-strain curves for shear. We generally observe

a tension-compression asymmetry with a peak compressive stress that is about 16% higher than the peak tensile stress. Additionally, we observe that adding cells had the largest impact on the asymmetry with about 19%.

Within the 10% uniaxial strain regime that we tested, compression and tension curves do not exhibit major nonlinearities. Loading up to 20% in shear, however, shows an increased nonlinear stress-strain behavior. Lastly, groups 1, 3, and 6 show more pronounced differences with respect to maximum stress between curves in comparison to the other groups which suggests that some printing parameters have a stronger impact on the material response of our constructs. Overall, we observe that the stiffest material behavior, i.e., maximum stress at maximum strain, when increasing GelMA concentration (group 4) and the softest response when adding cells to our constructs (group 6). In case of cell-free constructs, the softest behavior is observed when increasing the temperature of the GelMA (group 3).

3.2. Shear modulus variations based on support-bath printing configurations

Table 2 summarizes the model parameters for each printing configuration for the Neo-Hookean, Ogden, and Gent model. Specifically, we report the shear modulus and nonlinearity constant for the fit against the averaged stress-strain response across all three samples per printing configuration as well as the minimum and maximum shear modulus (and their corresponding nonlinearity constants) based on fits of each individual sample. Across all printing conditions ($n=18$), we observe a mean construct shear stiffness of 0.25 ± 0.14 kPa for the Neo-Hookean model, 0.23 ± 0.11 kPa for the Ogden model (with a nonlinearity constant α of 15.77 ± 3.28), and 0.25 ± 0.14 kPa for the Gent model (with a nonlinearity constant J_m of 10.14 ± 0.38). Those values are significantly lower than the stiffness observed for the in-air printed constructs which are about 8.7 times stiffer with a shear stiffness of 2.18 kPa for the Neo-Hookean model, 1.75 kPa for the Ogden model (with α 26.18), and 2.21 kPa for the Gent model (J_m 20.71). We generally observe similar shear moduli per printing condition across all three constitutive models. Stiffness changes based on increasing/decreasing printing parameters are also consistently reflected in shear modulus trends across models.

Fig. 3 compares shear moduli of the Neo-Hookean, Ogden, and Gent model, respectively, and indicates statistical significance between printing conditions. We only observe statistical significant differences in the shear moduli for printing configurations of groups 1, 3, 4, and 6. Notably, elevating the support bath temperature (group 1) from 4 °C to 37 °C results in a significant reduction of the shear modulus by 63%. Increasing GelMA temperature (group 3) from 24 °C to 37 °C also causes a statistically significant drop of the shear modulus by 45%. Ultimately, however, GelMA concentration (group 4) has the most significant impact on sample stiffness across all other printing parameters. Doubling GelMA concentration leads to a 200% modulus increase. Lastly, seeding cells in the GelMA ink, to produce what we refer to as bioink (group 6), causes sample stiffness to drop. We observe significant differences between various groups and an average 32% stiffness drop each time we doubled cell numbers.

Fig. 4 compares nonlinearity constants α from the Ogden model and J_m from the Gent model, respectively, and indicates statistical significance within each group of printing parameters. We generally observe that J_m shows significantly less variation within printing groups in comparison to α from the Ogden model. Group 3, i.e., GelMA temperature, is the only case where we observe a statistical significance between the Gent model's J_m for the two printing conditions at 24 °C and 37 °C. This indicates that the nonlinearity of our models is rather consistent across all printing conditions and marginally affects material response.

In contrast to most other studies that just fit a single loading mode at a time, we fit all three loading modes simultaneously. Although this generally leads to a worse fit for individual models, it ensures

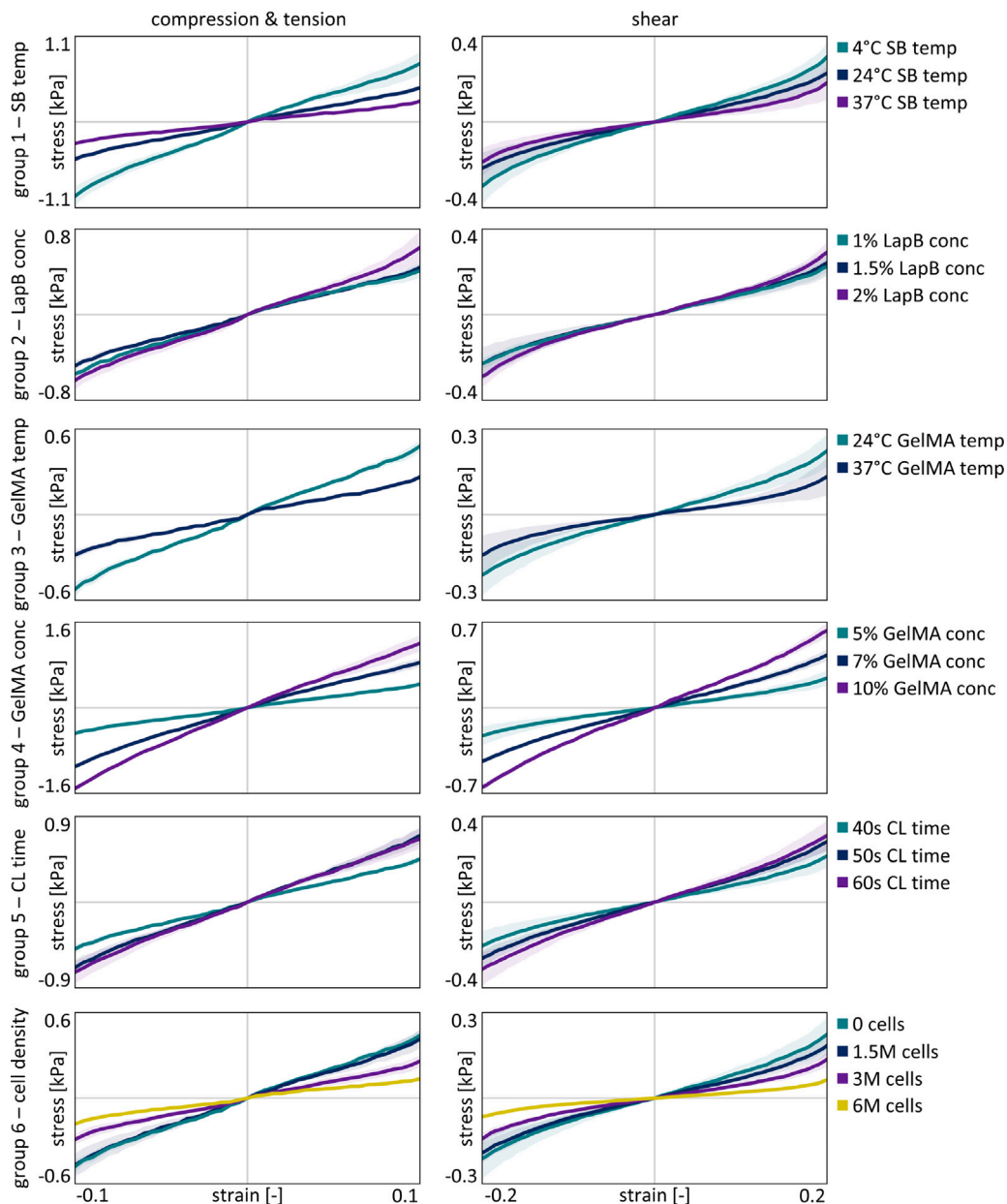


Fig. 2. Averaged stress–strain curves across all six groups: support bath (SB) temperature, LaponiteB (LapB) concentration, GelMA temperature, GelMA concentration, crosslinking time (CL), and cell density. We applied up to 10% strain in both compression and tension as well as up to $\pm 20\%$ strain in shear. Note that the stress range varies between plots.

that our parameters provide a robust approximation of the overall material response. In the supplemental materials, we report the results of our fits using the three different constitutive models as well as the corresponding relative square error for compression, tension, and shear separately. Specifically, we evaluate the goodness of fit of our compression, tension, and shear data using a single set of optimized model parameters. For the Neo-Hookean model we observe an average RSE of 0.23 in tension, 0.36 in compression, and 1.05 in shear which suggests a good approximation of the material’s response (see Tab. S1 in the supplementary materials). Similarly, the Gent model also provides robust fits with an average RSE of 0.26 in tension, 0.32 in compression, and 1.14 in shear (see Tab. S2 in supplementary materials). For the Ogden model, however, we observe poorer overall fits with an average RSE of 1.04 in tension, 0.51 in compression, and 0.97 in shear (see Tab. S3 in supplementary materials). These results suggest that the Neo-Hookean and Gent model are both better at capturing the response of our cell-laden GelMA constructs than the stretch-based Ogden model. For illustration purposes, Figs. S1-S3 in the supplemental

materials show the averaged stress–strain curves across all six groups against the results from the Neo-Hookean, Ogden, and Gent models. This shows how our fits provide reliably good approximations of the experimentally observed behavior.

3.3. Support-bath vs. in-air printed construct stiffness

Traditional printing bioprinting methods continue to be performed in air. We prepared multiple samples using the same in-air printing parameters, see Table 2, that allowed to print the softest-possible constructs that were true to the prescribed geometry, i.e., did not collapse under their own weight. Fig. 5 shows the stress–strain curves in (a) compression and tension as well as in (b) shear of the softest (blue) and stiffest (purple) support bath printed constructs in comparison to the in-air printed curves (green). Interestingly, we observe less tension–compression asymmetry but increased nonlinearity in the shear response. Based on our parameter identification, we obtain shear moduli for in-air printed constructs of 2.18 kPa for the Neo-Hookean

Table 2

Model parameters for the Neo-Hookean (μ), Ogden (μ, α), and Gent model (μ, J_m) based on fitting the averaged stress–strain response from all three samples of each printing configuration. In addition, we show the minimum and maximum shear stiffness value (and corresponding nonlinearity constants for the Ogden and Gent model) based on fitting the stress–strain response of each sample individually. Moreover, we provide the relative square error (RSE) of the average fit for comparison of the goodness of fit between printing conditions.

	Neo-Hookean			Ogden			Gent		
	μ [kPa] (min ; max)	RSE	μ [kPa] (min ; max)	α [-] (min ; max)	RSE	μ [kPa] (min ; max)	J_m [-] (min ; max)	RSE	
Support bath printing parameter configurations									
G1	4 °C	0.36 (0.20 ; 0.42)	1.46	0.29 (0.14 ; 0.42)	15.97 (1.01 ; 18.86)	3.04	0.36 (0.21 ; 0.43)	10.56 (10.23 ; 11.24)	2.71
	24 °C	0.22 (0.18 ; 0.23)	1.42	0.20 (0.15 ; 0.22)	18.18 (5.88 ; 18.19)	2.48	0.22 (0.18 ; 0.23)	9.76 (9.49 ; 10.01)	1.43
	37 °C	0.13 (0.11 ; 0.16)	2.56	0.13 (0.09 ; 0.21)	16.21 (14.13 ; 18.49)	3.65	0.16 (0.11 ; 0.25)	10.16 (10.22 ; 10.23)	2.84
G2	1.0%	0.23 (0.21 ; 0.24)	1.61	0.19 (0.16 ; 0.20)	17.05 (17.69 ; 18.36)	2.17	0.23 (0.21 ; 0.24)	10.11 (10.66 ; 10.85)	1.61
	1.5%	0.22 (0.18 ; 0.23)	1.42	0.20 (0.15 ; 0.22)	18.18 (5.88 ; 18.19)	2.48	0.22 (0.18 ; 0.23)	9.76 (9.49 ; 10.01)	1.43
	2.0%	0.27 (0.22 ; 0.30)	3.03	0.24 (0.18 ; 0.25)	16.74 (14.26 ; 19.21)	3.17	0.27 (0.22 ; 0.30)	10.69 (10.66 ; 10.69)	3.01
G3	24 °C	0.22 (0.18 ; 0.23)	1.42	0.20 (0.15 ; 0.22)	18.18 (5.88 ; 18.19)	2.48	0.22 (0.18 ; 0.23)	9.76 (9.49 ; 10.01)	1.43
	37 °C	0.12 (0.09 ; 0.11)	1.49	0.12 (0.07 ; 0.10)	8.18 (11.61 ; 18.16)	1.23	0.11 (0.09 ; 0.11)	10.77 (20.58 ; 20.61)	1.50
G4	5.0%	0.22 (0.18 ; 0.23)	1.42	0.20 (0.15 ; 0.22)	18.18 (5.88 ; 18.19)	2.48	0.22 (0.18 ; 0.23)	9.76 (9.49 ; 10.01)	1.43
	7.0%	0.47 (0.44 ; 0.48)	0.97	0.44 (0.37 ; 0.46)	15.59 (2.12 ; 20.51)	1.67	0.45 (0.46 ; 0.49)	10.85 (9.43 ; 10.66)	0.97
	10.0%	0.66 (0.60 ; 0.69)	0.96	0.50 (0.42 ; 0.51)	13.56 (17.61 ; 21.15)	3.91	0.65 (0.60 ; 0.70)	10.25 (9.89 ; 10.66)	0.96
G5	40 s	0.22 (0.18 ; 0.23)	1.42	0.20 (0.15 ; 0.22)	18.18 (5.88 ; 18.19)	2.48	0.22 (0.18 ; 0.23)	9.76 (9.49 ; 10.01)	1.43
	50 s	0.31 (0.25 ; 0.34)	2.17	0.27 (0.21 ; 0.33)	20.31 (5.23 ; 18.77)	1.75	0.31 (0.25 ; 0.34)	9.88 (10.13 ; 10.16)	1.99
	60 s	0.33 (0.25 ; 0.37)	1.56	0.30 (0.25 ; 0.36)	14.55 (4.61 ; 15.03)	3.02	0.35 (0.25 ; 0.37)	10.16 (10.16 ; 10.24)	1.58
G6	0 Cells	0.22 (0.18 ; 0.23)	1.42	0.20 (0.15 ; 0.22)	18.18 (5.88 ; 18.19)	2.48	0.22 (0.18 ; 0.23)	9.76 (9.49 ; 10.01)	1.43
	1.5M	0.19 (0.16 ; 0.23)	1.47	0.19 (0.13 ; 0.23)	9.61 (11.98 ; 17.86)	1.61	0.19 (0.16 ; 0.24)	9.93 (9.79 ; 10.01)	1.48
	3.0M	0.13 (0.12 ; 0.13)	2.18	0.12 (0.11 ; 0.12)	15.97 (12.58 ; 17.58)	2.57	0.12 (0.12 ; 0.13)	10.26 (9.99 ; 10.01)	2.19
	6.0M	0.06 (0.05 ; 0.07)	1.59	0.06 (0.05 ; 0.06)	11.02 (9.37 ; 12.45)	2.10	0.06 (0.05 ; 0.07)	10.27 (9.95 ; 10.02)	1.59
In-air printing parameter configurations									
G7	2.18 (1.8 ; 2.44)	4.14	1.75 (1.57 ; 1.76)	26.18 (15.69 ; 22.77)	4.56	2.21 (1.82 ; 2.47)	20.71 (16.69 ; 18.72)	4.85	

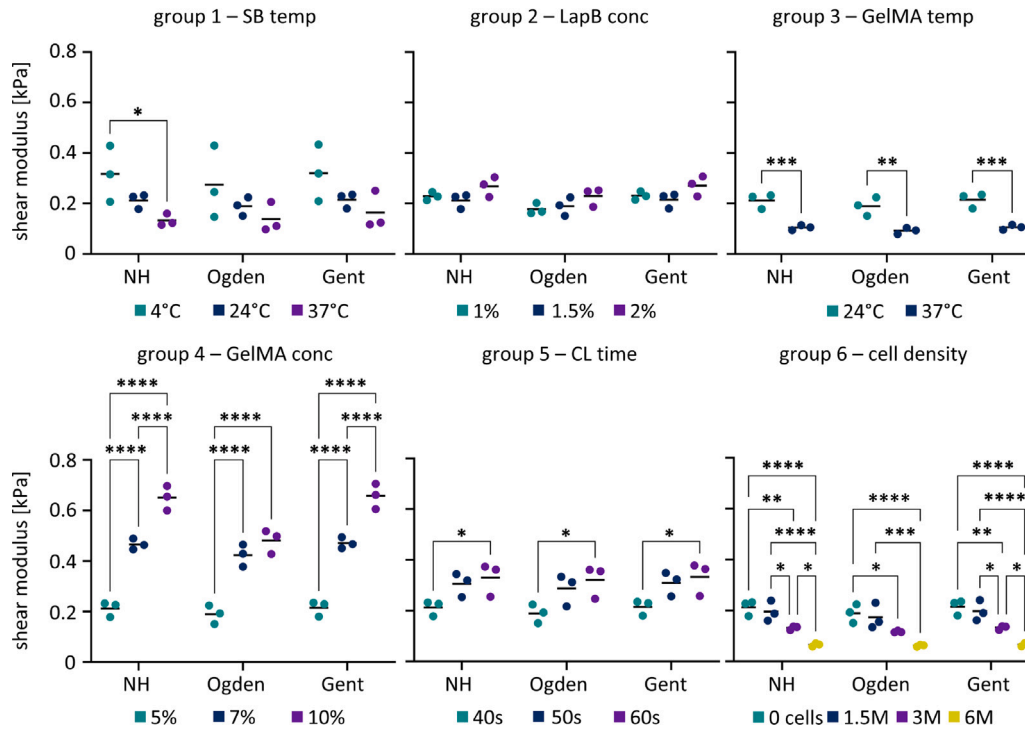


Fig. 3. Shear moduli of support bath printed constructs for the Neo-Hookean, Ogden, and Gent models. Each point represents the shear modulus of a single sample and the horizontal black line indicates the shear modulus reported in Table 2 which is based on the averaged stress–strain behavior across all three samples per printing condition. We statistically analyzed intra-group variations and indicate $p < 0.05$ with *, $p < 0.01$ with **, $p < 0.001$ with ***, and $p < 0.0001$ with ****. In this context, SB denotes the support bath, LapB refers to LaponiteB, and CL stands for cross-linking time.

model, 1.75 kPa for the Ogden model (with nonlinearity constant α of 26.18), and 2.21 kPa for the Gent model (with nonlinearity constant J_m of 20.71). In general, the average shear modulus, see Fig. 5(c), of in-air printed constructs is 22-times stiffer than the softest and up to 3.5-times stiffer than the stiffest support-bath printed constructs, respectively.

Based on comparison for each hyperelastic model respectively, we observe statistically significant differences between the shear moduli for all three printing conditions. However, the choice of hyperelastic model has a minor impact on the shear modulus which is reflected in similar values for the three different printing conditions, respectively.

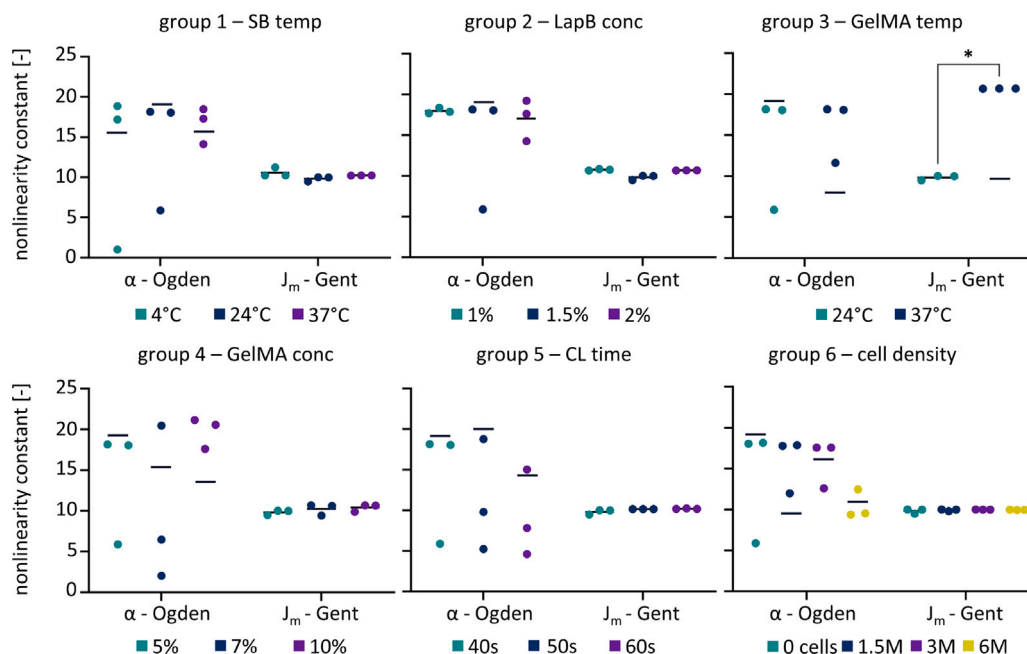


Fig. 4. Nonlinearity constants of support bath-based printed constructs for the Ogden and Gent models. Each point represents the nonlinearity constant from the fit of a single sample and the horizontal black line indicates the nonlinearity constant reported in Table 2 which is based on the averaged stress–strain behavior across all three samples per printing condition. We statistically analyzed intra-group variations and indicate $p < 0.05$ with *, $p < 0.01$ with **, $p < 0.001$ with ***, and $p < 0.0001$ with ****. In this context, SB denotes the support bath, LapB refers to LaponiteB, GelMA represents gelatin methacryloyl, and CL stands for cross-linking time.

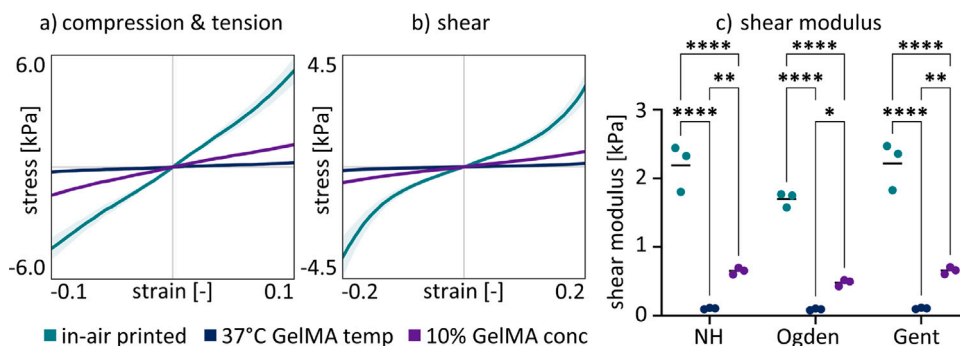


Fig. 5. Comparison of the stress–strain curves in (a) compression and tension and in (b) shear as well as (c) the shear moduli for the softest support bath printed, stiffest support bath printed, and in-air printed constructs, respectively. Each point represents the shear modulus from the fit of a single sample and the horizontal black line indicates the shear modulus reported in Table 2 which is based on the averaged stress–strain behavior across all three samples per printing condition. We statistically analyzed the effect of printing condition on shear modulus and indicate $p < 0.05$ with *, $p < 0.01$ with **, $p < 0.001$ with ***, and $p < 0.0001$ with ****.

3.4. Cell live/Dead assays

Figs. 6a-c shows the results of the live/dead assay for the in-air printed constructs (7% GelMA printed at 21 °C), softest constructs (5% GelMA printed at 37 °C), and stiffest constructs (10% GelMA printed at 24 °C). In our fluorescent staining, live cells appear green and dead cells appear red. The merged image indicates cell density distributions. Fig. 6d compares cell viability for these three printing conditions. Average cell viability, i.e., fraction of live-to-dead cells averaged across the three samples, of the in-air printed construct seeded with 1.5 million cells, drops to 71.28% by the third day, then recovers by 8% by day 5, and ultimately drops to 48.1% by the end of the 7-day observation period. For the softest support-bath printed construct seeded with 1.5 million cells, average cell viability first decreases to 95.85% by day three, then drops by about 20% by day 5, and ultimately stabilizes around 73% for the remaining observation period. For the stiffest support-bath printed construct seeded with 1.5 million cells, average cell viability drops to 78% within the first three days and remains at a similar level of 74.06% and 80.55% by days 5 and 7, respectively. While there are no significant differences in cell viability

between days 5 and 7, a notable difference is observed between the initial day of cell seeding and day 3. After an initial decline, where the live cell count drops by no more than 25%, cell viability appears to stabilize. The cell viability of the in-air printed construct shows a significant difference only when compared to the softest construct on day 3. However, by day 7, there is a significant difference in cell viability between the in-air printed construct when compared to both the softest and stiffest support-bath printed constructs.

4. Discussion

4.1. Effect of material and printing parameters on construct stiffness

GelMA bioink has been extensively investigated in recent years (Banerjee et al., 2021; Sharifi et al., 2021) and has exhibited substantial stiffness variations as a function of polymer concentration (Pepelanova et al., 2018), crosslinking density (Sharifi et al., 2021), crosslinking time (Karaoglu et al., 2023), and printing temperature (Zhu et al., 2019). Owing to its high biocompatibility, GelMA has emerged as

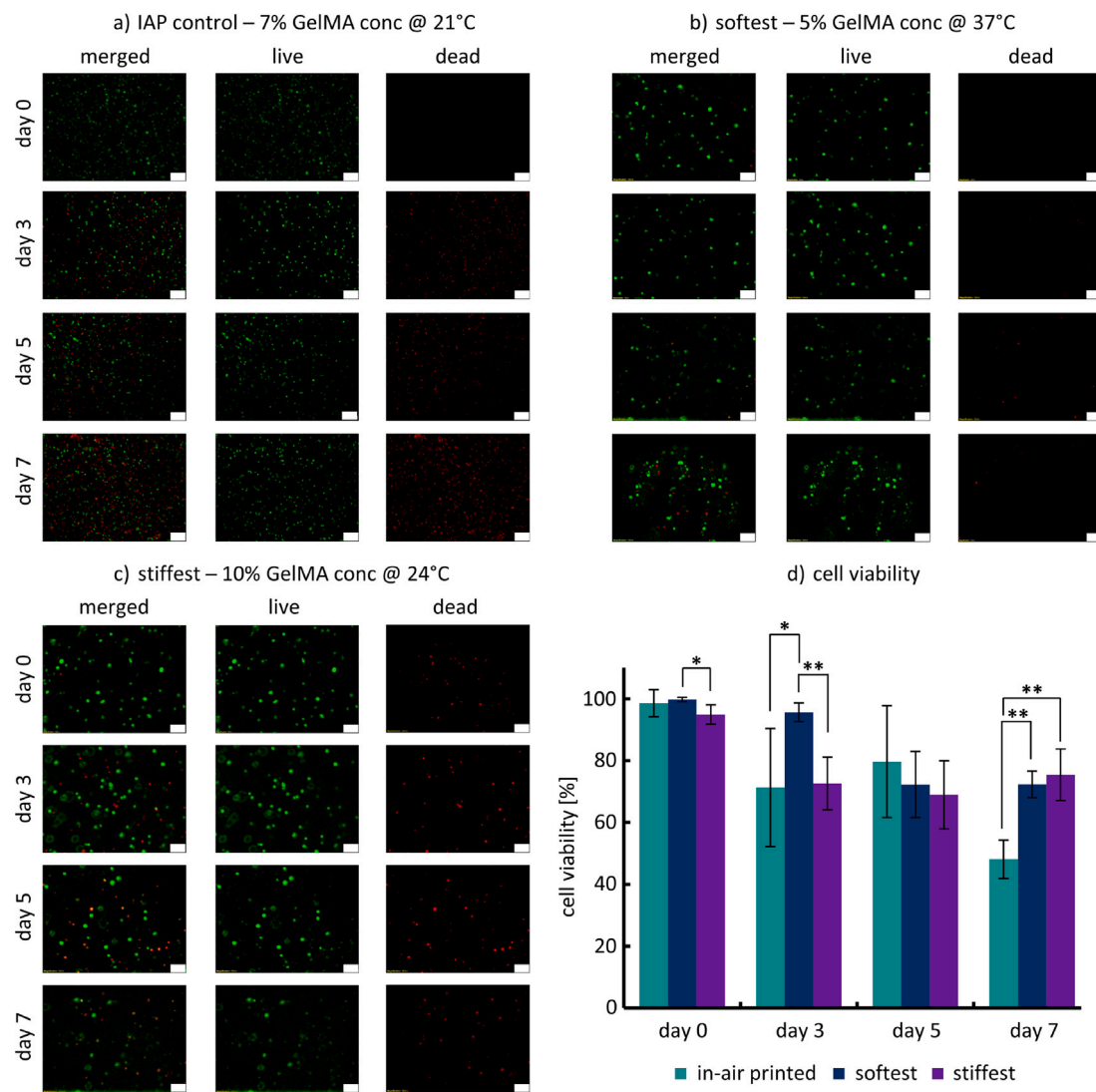


Fig. 6. Summary of cell viability assessment for in-air printed in comparison to the softest and stiffest support bath printed GelMA constructs at specified concentrations and temperatures over a period of 7 days: representative live/dead cell assay images of (a) in-air printed constructs with 7% GelMA concentration maintained at 21 °C, (b) softest support bath printed construct with 5% GelMA concentration maintained at 37 °C, and (c) stiffest support bath printed construct with 10% GelMA concentration at 24 °C; (d) cell viability for the three printing conditions at days 0, 3, 5, and 7, respectively. Statistical significance is denoted by * for $p < 0.05$, by ** for $p < 0.01$, and by *** for $p < 0.001$. Magnification of the images is 12x, and the scale bars are 50 μm .

a prominent matrix material for cell-laden bioinks (Rajabi et al., 2021; Boularaoui et al., 2021; Gungor-Ozkerim et al., 2018). Our support bath material contains LaponiteB, a synthetic disc-shaped clay nanoparticle, known for its property to enhance overall structural integrity (Ding and Chang, 2018; Ding et al., 2019). Factors such as LaponiteB concentration, the degree of nanoparticle dispersion within the hydrogel (Zheng et al., 2020), crosslinking density, and support bath temperature (Afghah et al., 2020) contribute to the intrinsic viscosity and stiffness of the support bath material. Based on Fig. 4, we observe that GelMA concentration, temperature, and cell density have a statistically significant effect on construct stiffness; support bath temperature and UV crosslinking time have a weak ($p < 0.05$) effect on construct stiffness; and LaponiteB concentration in the support bath is observed to show no direct effect on construct properties.

Higher GelMA concentrations generally yield a higher construct stiffness due to increased structural integrity resulting from a denser matrix and smaller pore sizes (Kulkarni et al., 2022). Varying GelMA printing temperature also leads to statistically significant construct stiffness differences (Young et al., 2020; Janmaleki et al., 2020). Specifically, increasing GelMA temperature results in a softer construct response which we attribute to heat-sensitive hydrogen bonds in gelatin

that reduce overall structural connectivity (Sun et al., 2018). By extension, support bath temperature primarily affects the overall temperature of the hydrogel mixture. A support bath temperature of 4 °C inherently lowers GelMA temperature during the printing process and, therefore, increases its overall stiffness. A support bath temperature of 24 °C and higher contributes to a loss in bond strength and decreases overall construct stiffness (Sun et al., 2018). Interestingly, despite an approximate 50% increase in average construct stiffness in group 5, we observe only weak statistically significant differences when extending crosslinking time from 40 to 60 s. Generally, extending curing time not only promotes further crosslinking within the polymer network but also leads to the formation of additional covalent bonds, thereby enhancing the stiffness and overall structural strength of the GelMA matrix (Sharifi et al., 2021). We suspect that for our low-concentration hydrogels, GelMA concentrations are so low that fewer additional covalent bonds are formed passed the 40 s mark. Lastly, the concentration of LaponiteB in the support bath exhibits a minor influence on construct stiffness, a phenomenon we ascribe to its role in supporting the printing process rather than any direct chemical interaction with the GelMA material (Hua et al., 2022).

In previous work (Ding and Chang, 2018), we established that a 5% GelMA concentration combined with a UV crosslinking time of 40 s yields a balanced outcome between stability and compliance needed to replicate the lower range of stiffnesses typical for vascular tissues (Kohn et al., 2015). This deliberate selection of material conditions reflects the mechanical gradients observed in vascular systems, where a softer endothelial layer is juxtaposed with the stiffer outer structural layers (Wang et al., 2016; Fonck et al., 2009). Given common stiffness ranges of soft tissues, we chose to test GelMA concentrations ranging from 5% to 10%, as well as UV crosslinking times between 40 and 60 s. Based on these printing conditions, we were able to show that our constructs preserve integrity and are soft enough to support cellular health and functionality, a critical aspect for biomedical applications (Ding et al., 2019; Xu et al., 2022).

4.2. Increasing cell density decreases construct stiffness

Increasing cell density in our bioink significantly decreases overall construct stiffness by up to 67%. We attribute this softening behavior to the displacement of GelMA material with live cells whereby the drop in GelMA volume fraction reduces the amount of crosslinking during the curing process. Prior studies have established, that increments in the prescribed cell density yields larger hydrogel matrix pore sizes and a weaker hydrogel matrix structure (Krishnamoorthy et al., 2019; Yin et al., 2023). In addition, changes in the material's porosity affect its water retention capacity and osmotic balance (Miri et al., 2018). These corresponding alterations in the water composition invariably affect both elastic stiffness and time-dependent material behavior of the printed construct (Chalard et al., 2022). To that end, it has been shown that the interactions between cells and GelMA hydrogel are dynamic and alter hydrogel microstructure over time (Yin et al., 2023). Cells actively remodel hydrogel matrix through the release of metabolic byproducts and secretion of enzymes that degrade the gelatin-based components of GelMA (Nikkhah et al., 2012). Furthermore, cells exert mechanical forces on the hydrogel matrix, thus altering its architecture with direct implications on pore sizes and stiffness (Bova et al., 2023). Besides mechanical forces, biochemical cues influence degradation rate and crosslinking density. In the case of relatively long duration time courses for incubation, proliferating cells deposit extracellular matrix components within the hydrogel which contributes to structural and mechanical property changes (Chaudhuri et al., 2020). As cells grow and start producing extracellular matrix within the GelMA, the constructs are expected to become softer over time. This is due to the increasing cell density, which influences the mechanical properties by creating a more cell-dominated matrix. Our results strengthen this explanation given the increased GelMA softening with increased cell concentration.

Our study shows strong cell viability across a 7-day observation window in both our softest and stiffest constructs — especially, when compared to our in-air printed construct that used common printing parameters, see Fig. 6. For the support bath printed constructs, cell viability initially declines, then stabilizes by day 5. For the in-air printed construct, we observe much lower cell viability, in general, and no stabilization of live cell count within the 7 day observation period.

Our findings indicate that the support bath-based printing approach allows to fabricate constructs with mechanical properties soft enough to be conducive to survival and proliferation of endothelial cells (Shie et al., 2020). Specifically for endothelial cells, it is noted that while stiffer constructs may promote higher proliferation rates (Zamani et al., 2022; Wei et al., 2023), there is a marked preference for bioinks with lower stiffness in research scenarios that necessitate rapid degradation and precise control over cellular invasion (Ding et al., 2019; Yeung et al., 2005). This underscores the importance of tailoring the mechanical properties of bioinks to meet the specific requirements for any biological studies that will be done. To that end, in-air printed constructs are inherently stiffer, in part simply to maintain structural

integrity of more complex structures such as a hollow cylinder. The resulting environment, however, lowered cell survival in our study. The cells' ability to sense their surrounding mechanical environment via mechanoreceptors enables them to dynamically respond to changes in their microenvironment (Puech and Bongrand, 2021). Environments representative of the *in vivo* mechanical profile of soft tissues promote cell viability, growth, and the deposition of extracellular matrix in support of long-term feasibility of cell-laden constructs (Hu et al., 2021; Lin et al., 2018).

4.3. Support-bath printing enables soft specialized constructs

Interest in high-fidelity fabrication of 3D cell-laden hydrogel structures mimicking native tissues and organs is rapidly growing (Mota et al., 2020). There exists an intrinsic challenge, however, between approximating the soft nature of biological tissues and creating complex construct geometries that preserve shape and mechanical integrity (Schwab et al., 2020). This is particularly evident in the presence of cells, which gradually remodel the hydrogel microstructure. We attribute this to the hydrogel-based constructs degenerating faster than cells can deposit sufficient extracellular matrix to preserve shape causing a significant decline in mechanical integrity (Hull et al., 2022). Promoting long-term stability is critical for developing medically useful engineered tissue applications. Thus far, only high-concentration bioinks have had sufficiently high viscosity to confer structural stability during sequential layering (Jin et al., 2017; Zhang et al., 2018). These high-density polymer networks, however, serve to limit essential cellular functions, such as spreading, migration, and proliferation, and present an environmental stiffness that is incompatible with cells of soft-tissue origin (Ouyang et al., 2020).

Recent innovations in support bath printing techniques have expanded the variety of available bioinks and allowed the biofabrication of constructs optimized to meet the biological requirements of cell culture and tissue engineering. Specifically, providing a structural support during the printing process and the ability to extract cell-laden hydrogel constructs after curing makes support baths an intriguing alternative. As such, several recent studies have presented shapes ranging from lattices and grid-like structures to more elaborate 3D structures mimicking hollow cubes, vessel-like structures, pyramids, and hollow drums (Hinton et al., 2015; Afghah et al., 2020; Ning et al., 2020; Ji and Guvendiren, 2021).

All that being said, no standardized methods for fabrication and mechanical characterization of hydrogels exist today. That makes comparison between studies difficult and limits our ability to define printing conditions that deliver constructs with desired properties. Moreover, most studies presented in literature rely on rheological experiments which characterize tissues under compressive and shear loading and not under more physiological conditions that may include tensile and multiaxial loading (Blache et al., 2022). Literature provides numerous studies exploring the stiffness of various types of hydrogels based on different testing protocols (Wu et al., 2019; Adib et al., 2020; Costantini et al., 2017). Wu et al. conducted uniaxial tensile tests on rectangular GelMA samples using an ElectroForce (TA Instruments, USA) system (Wu et al., 2019). They measured Young's moduli ranging from 3 to 185 kPa based on uniaxial tensile tests up to 25% strain Wu et al. (2019). Adib et al. performed cyclic tensile tests on dogbone-shaped GelMA samples using an Instron 3344 (Norwood, MA, USA) (Adib et al., 2020). They reported Young's moduli ranging from 100 to 160 kPa with maximum tensile stresses of 20 to 25 kPa at 20% strain. Costantini et al. carried out unconfined compression tests on cylindrical GelMA samples using an Instron 3365 (Norwood, MA, USA) (Costantini et al., 2017). They reported substantially lower Young's moduli of 1 to 16 kPa at 20% compressive strain. It is quite evident that stiffness values range substantially and depend on a large number of factors. Our testing approach provides insight into the rich 3D deformation state, ranging from quasi-static to cyclic loading profiles. While our current analyses

were limited to a hyperelastic material response, our method provides extensive insight into the tension–compression asymmetry and shear behavior of constructs. By using an inverse approach, we determine a single model parameter set that best represents all three loading conditions rather than limiting ourselves to capturing each model individually.

Mechanical properties of biological tissues vary substantially with values ranging from hundreds of Pascals in the example of mucus to several gigapascals in bone (Guimarães et al., 2020). Our constructs have an overall average stiffness of 0.401 ± 0.54 kPa and fall well within that range. Additionally, our values are comparable to the stiffness of individual cells (± 1 kPa) (Luo et al., 2016), but of many tissues and organs (~ 1 – 10 kPa), such as the brain, cardiac tissues, and lung (Guimarães et al., 2020), as well. Our construct geometry is primarily designed to vaguely mimic vasculature although we grossly simplify its complex anatomy by simply creating hollow cylinders. Real vasculature is made up of three layers: The outer adventitia layer which provides structural support and shape to the vessel; the media or middle layer composed of elastic and muscular tissue which regulates the internal diameter of the vessel; and the intima, or an inner layer, consisting of an endothelial lining which provides a frictionless pathway for the movement of blood (Holzapfel et al., 2000). This anatomy gives rise to highly functional properties that are expected to differ significantly from our observations here and would require a different testing approach such as inflation-extension testing. We observe, for example, that in comparison to our constructs, vessels are significantly stiffer (~ 50 kPa)—mostly due to their high collagen content and highly anisotropic material response that is optimized to sustain blood pressures between 70 mmHg during diastole and 130 mmHg during systole (Camasão and Mantovani, 2021).

4.4. Limitations

Our study is not without limitations. For one, our construct's hollow cylinder geometry may be inspired by arterial tissue but they clearly lack their intricate functional capabilities as well as highly anisotropic, viscoelastic material behavior. For the other, our triaxial testing machine is not the most suited setup to explore the mechanical properties of a tubular structure. For example, inflation-extension tests are much more common in determining the mechanical properties of arteries and vessels (Camasão and Mantovani, 2021). In the bioprinting-focused work here, we primarily aim to study the effect of critical printing parameters on the overall mechanical properties before working towards better tissue-mimics. Lastly, our tests are conducted in air rather than in a water bath. Therefore, we developed a protocol such that the time between removing a sample from the support bath and completing all its experimental tests is less than 10 min. We pose that this time frame is too short to substantially affect the construct's mechanical behavior. Nonetheless, future work should aim to assess the impact of a water bath on the mechanical response of our bioprinted constructs.

5. Conclusion

Our study explored the effects of various material and printing parameters on the stiffness of tubular low-concentration GelMA constructs fabricated via the support bath printing method. By combining multiaxial mechanical testing and inverse finite element analysis, we were able to show that the stiffness of our tubular constructs varies between 0.07 and 2.2 kPa which matches the stiffness of many cells and tissues. The beneficial mechanical environment of our soft constructs is reflected in a very high cell survival rate of around 85% across a 7-day observation period. This research not only enhances our understanding of the impact of printing parameters on the mechanical properties of bioprinted constructs but also paves the way for the ongoing development of bioprinting protocols to create complex tissue-mimicking constructs.

Funding

Dr. Robert Chang received funding from the National Science Foundation under Award No. CMMI-MME-1663095, the U.S. Army Medical Research Acquisition Activity under Award No. USAMRAA-W81XWH-19-1-0158, and the New Jersey Health Foundation under Award No. PC59-23. Dr. Johannes Weickenmeier received funding from the National Science Foundation under Award No. CMMI-1953323 and the Frank Semcer, Sr. '65 Fellowship.

CRediT authorship contribution statement

Ahsanul Torza: Writing – original draft, Visualization, Formal analysis, Data curation. **Ralf Zgeib:** Writing – original draft, Visualization, Data curation. **Xiaofeng Wang:** Writing – original draft, Data curation. **Ahmadreza Zaeri:** Writing – original draft, Data curation. **Fucheng Zhang:** Writing – original draft, Data curation. **Kai Cao:** Writing – original draft, Data curation. **Robert Chang:** Writing – original draft, Investigation, Funding acquisition, Conceptualization. **Johannes Weickenmeier:** Writing – review & editing, Methodology, Investigation, Funding acquisition, Conceptualization.

Declaration of competing interest

The authors declare that the research was conducted in the absence of any commercial or financial relationships that could be construed as a potential conflict of interest.

Data availability

Data will be made available on request.

Appendix A. Supplementary data

Supplementary material related to this article can be found online at <https://doi.org/10.1016/j.ijsolstr.2024.112938>.

References

- Aadib, A.A., Sheikhi, A., Shahhosseini, M., Simeunović, A., Wu, S., Castro, C., Zhao, R., Khademhosseini, A., Hoelzle, D., 2020. Direct-write 3d printing and characterization of a gelma-based biomaterial for intracorporeal tissue engineering. *Biofabrication* 12, 045006.
- Afghah, F., Altunbek, M., Dikyol, C., Koc, B., 2020. Preparation and characterization of nanoclay-hydrogel composite support-bath for bioprinting of complex structures. *Sci. Rep.* 10, 5257.
- Ahmadi Soufivand, A., Faber, J., Hinrichsen, J., Budday, S., 2023. Multilayer 3d bioprinting and complex mechanical properties of alginate-gelatin mesostructures. *Sci. Rep.* 13, 11253.
- Ansari, S., Sarrion, P., Hasani-Sadrabadi, M.M., Aghaloo, T., Wu, B.M., Moshaverinia, A., 2017. Regulation of the fate of dental-derived mesenchymal stem cells using engineered alginate-gelma hydrogels. *J. Biomed. Mater. Res. A* 105, 2957–2967.
- Banerjee, A., Datta, S., Chowdhury, A.R., Datta, P., 2021. A finite element analysis model to predict and optimize the mechanical behaviour of bioprinted scaffolds. *arXiv preprint arXiv:2103.05721*.
- Bessot, A., Gunter, J., Waugh, D., Clements, J.A., Hutmacher, D.W., McGovern, J., Bock, N., 2023. Gelma and biomimetic culture allow the engineering of mineralized, adipose, and tumor tissue human microenvironments for the study of advanced prostate cancer in vitro and in vivo. *Adv. Healthc. Mater.* 12, 2201701.
- Blache, U., Ford, E.M., Ha, B., Rijns, L., Chaudhuri, O., Dankers, P.Y., Kloxin, A.M., Snedeker, J.G., Gentleman, E., 2022. Engineered hydrogels for mechanobiology. *Nat. Rev. Methods Primers* 2, 98.
- Boularaoui, S., Shanti, A., Lanotte, M., Luo, S., Bawazir, S., Lee, S., Christoforou, N., Khan, K.A., Stefanini, C., 2021. Nanocomposite conductive bioinks based on low-concentration gelma and mxene nanosheets/gold nanoparticles providing enhanced printability of functional skeletal muscle tissues. *ACS Biomater. Sci. Eng.* 7, 5810–5822.
- Bova, L., Maggiotto, F., Micheli, S., Giomo, M., Sgarbossa, P., Gagliano, O., Falcone, D., Cimetta, E., 2023. A porous gelatin methacrylate-based material for 3d cell-laden constructs. *Macromol. Biosci.* 23, 2200357.

- Brunel, L.G., Hull, S.M., Heilshorn, S.C., 2022. Engineered assistive materials for 3d bioprinting: support baths and sacrificial inks. *Biofabrication* 14, 032001.
- Budday, S., Sommer, G., Haybaeck, J., Steinmann, P., Holzapfel, G.A., Kuhl, E., 2017. Rheological characterization of human brain tissue. *Acta Biomaterialia* 60, 315–329.
- Camasão, D., Mantovani, D., 2021. The mechanical characterization of blood vessels and their substitutes in the continuous quest for physiological-relevant performances, a critical review. *Mater. Today Bio* 10, 100106.
- Castilho, M., Hochleitner, G., Wilson, W., Van Rietbergen, B., Dalton, P.D., Groll, J., Malda, J., Ito, K., 2018. Mechanical behavior of a soft hydrogel reinforced with three-dimensional printed microfibre scaffolds. *Sci. Rep.* 8, 1245.
- Chalard, A.E., Dixon, A.W., Taberner, A.J., Malmström, J., 2022. Visible-light stiffness patterning of gelma hydrogels towards in vitro scar tissue models. *Front. Cell Dev. Biol.* 10, 946754.
- Chaudhuri, O., Cooper-White, J., Janmey, P.A., Mooney, D.J., Shenoy, V.B., 2020. Effects of extracellular matrix viscoelasticity on cellular behaviour. *Nature* 584, 535–546.
- Costantini, M., Testa, S., Fornetti, E., Barbetta, A., Trombetta, M., Cannata, S.M., Gargioli, C., Rainer, A., 2017. Engineering muscle networks in 3d gelatin methacryloyl hydrogels: influence of mechanical stiffness and geometrical confinement. *Front. Bioeng. Biotechnol.* 5, 22.
- Ding, H., Chang, R.C., 2018. Printability study of bioprinted tubular structures using liquid hydrogel precursors in a support bath. *Appl. Sci.* 8, 403.
- Ding, H., Illsley, N.P., Chang, R.C., 2019. 3D bioprinted gelma based models for the study of trophoblast cell invasion. *Sci. Rep.* 9, 18854.
- Fonck, E., Feigl, G.G., Fasel, J., Sage, D., Unser, M., Rüfenacht, D.A., Stergiopoulos, N., 2009. Effect of aging on elastin functionality in human cerebral arteries. *Stroke* 40, 2552–2556.
- Gent, A.N., 1996. A new constitutive relation for rubber. *Rubber Chem. Technol.* 69, 59–61.
- Giolando, P., Kakaletsis, S., Zhang, X., Weickenmeier, J., Castillo, E., Dortdivanlioglu, B., Rausch, M.K., 2023. Ai-dente: an open machine learning based tool to interpret nano-indentation data of soft tissues and materials. *Soft Matter*.
- Guimarães, C.F., Gasperini, L., Marques, A.P., Reis, R.L., 2020. The stiffness of living tissues and its implications for tissue engineering. *Nat. Rev. Mater.* 5, 351–370.
- Gungor-Ozkerim, P.S., Inci, I., Zhang, Y.S., Khademhosseini, A., Dokmeci, M.R., 2018. Bioinks for 3d bioprinting: an overview. *Biomater. Sci.* 6, 915–946.
- Harding, A., Pramanik, A., Basak, A., Prakash, C., Shankar, S., 2023. Application of additive manufacturing in the biomedical field—a review. *Ann. 3D Printed Med.* 100110.
- Hinton, T.J., Jallerat, Q., Palchesko, R.N., Park, J.H., Grodzicki, M.S., Shue, H.-J., Ramadan, M.H., Hudson, A.R., Feinberg, A.W., 2015. Three-dimensional printing of complex biological structures by freeform reversible embedding of suspended hydrogels. *Sci. Adv.* 1, e1500758.
- Holzapfel, G.A., Gasser, T.C., Ogden, R.W., 2000. A new constitutive framework for arterial wall mechanics and a comparative study of material models. *J. Elasticity Phys. Sci. Solids* 61, 1–48.
- Hu, M., Jia, F., Huang, W.-P., Li, X., Hu, D.-F., Wang, J., Ren, K.-F., Fu, G.-S., Wang, Y.-B., Ji, J., 2021. Substrate stiffness differentially impacts autophagy of endothelial cells and smooth muscle cells. *Bioactive Mater.* 6, 1413–1422.
- Hua, W., Godina, B., Jin, Y., 2022. Liquid support bath-assisted 3 d bioprinting. *Cell Assembly 3D Bioprinting* 149–178.
- Hull, S.M., Brunel, L.G., Heilshorn, S.C., 2022. 3D bioprinting of cell-laden hydrogels for improved biological functionality. *Adv. Mater.* 34, 2103691.
- Janmaleki, M., Liu, J., Kamkar, M., Azarmanesh, M., Sundararaj, U., Nezhad, A.S., 2020. Role of temperature on bio-printability of gelatin methacryloyl bioink in two-step cross-linking strategy for tissue engineering applications. *Biomed. Mater.* 16, 015021.
- Ji, S., Guvendiren, M., 2021. Complex 3d bioprinting methods. *APL Bioeng.* 5.
- Jin, Y., Chai, W., Huang, Y., 2017. Printability study of hydrogel solution extrusion in nanoclay yield-stress bath during printing-then-gelation biofabrication. *Mater. Sci. Eng.: C* 80, 313–325.
- Jin, B., Liu, Y., Du, S., Sang, X., Yang, H., Mao, Y., 2022. Current trends and research topics regarding liver 3d bioprinting: A bibliometric analysis research. *Front. Cell Dev. Biol.* 10, 1047524.
- Kakaletsis, S., Meador, W.D., Mathur, M., Sugerman, G.P., Jazwiec, T., Malinowski, M., Lejeune, E., Timek, T.A., Rausch, M.K., 2021. Right ventricular myocardial mechanics: Multi-modal deformation, microstructure, modeling, and comparison to the left ventricle. *Acta Biomaterialia* 123, 154–166.
- Karaoglu, I.C., Kebabci, A.O., Kizilel, S., 2023. Optimization of gelatin methacryloyl hydrogel properties through an artificial neural network model. *ACS Appl. Mater. Interfaces* 15, 44796–44808.
- Klotz, B.J., Gawlitta, D., Rosenberg, A.J., Malda, J., Melchels, F.P., 2016. Gelatin-methacryloyl hydrogels: towards biofabrication-based tissue repair. *Trends Biotechnol.* 34, 394–407.
- Kohn, J.C., Lampi, M.C., Reinhart-King, C.A., 2015. Age-related vascular stiffening: causes and consequences. *Front. Genet.* 6, 112.
- Krishnamoorthy, S., Noorani, B., Xu, C., 2019. Effects of encapsulated cells on the physical-mechanical properties and microstructure of gelatin methacrylate hydrogels. *Int. J. Mol. Sci.* 20, 5061.
- Kulkarni, N.S., Chauhan, G., Goyal, M., Sarvepalli, S., Gupta, V., 2022. Development of gelatin methacrylate (gelma) hydrogels for versatile intracavitary applications. *Biomater. Sci.* 10, 4492–4507.
- Larsson, M., Kremer, F., Kuznetsova, T., Lind, B., Bjällmark, A., Brodin, L.-Å., D'hooge, J., In-vivo assessment of radial and longitudinal strain in the carotid artery using speckle tracking, in: 2010 IEEE International Ultrasonics Symposium, IEEE, pp. 1328–1331.
- Li, Y., Huang, G., Gao, B., Li, M., Genin, G.M., Lu, T.J., Xu, F., 2016. Magnetically actuated cell-laden microscale hydrogels for probing strain-induced cell responses in three dimensions. *NPG Asia Mater.* 8, e238.
- Li, Q., Ma, L., Gao, Z., Yin, J., Liu, P., Yang, H., Shen, L., Zhou, H., 2022. Regulable supporting baths for embedded printing of soft biomaterials with variable stiffness. *ACS Appl. Mater. Interfaces* 14, 41695–41711.
- Lin, A.P., Bennett, E., Wisk, L.E., Gharib, M., Fraser, S.E., Wen, H., 2008. Circumferential strain in the wall of the common carotid artery: Comparing displacement-encoded and cine mri in volunteers. *Magn. Resonance Med.: Off. J. Int. Soc. Magn. Resonance Med.* 60, 8–13.
- Lin, C.-H., Su, J.J.-M., Lee, S.-Y., Lin, Y.-M., 2018. Stiffness modification of photopolymerizable gelatin-methacrylate hydrogels influences endothelial differentiation of human mesenchymal stem cells. *J. Tissue Eng. Regenerative Med.* 12, 2099–2111.
- Luo, Q., Kuang, D., Zhang, B., Song, G., 2016. Cell stiffness determined by atomic force microscopy and its correlation with cell motility. *Biochim. Biophys. Acta (BBA)-General Subjects* (1860), 1953–1960.
- Maas, S.A., Ellis, B.J., Ateshian, G.A., Weiss, J.A., 2012. *Febio: finite elements for biomechanics*.
- Mancha Sánchez, E., Gómez-Blanco, J.C., López Nieto, E., Casado, J.G., Macías-García, A., Díaz Díez, M.A., Carrasco-Amador, J.P., Torrejón Martín, D., Sánchez-Margallo, F.M., Pagador, J.B., 2020. Hydrogels for bioprinting: A systematic review of hydrogels synthesis, bioprinting parameters, and bioprinted structures behavior. *Front. Bioeng. Biotechnol.* 8, 776.
- Mandrycky, C., Wang, Z., Kim, K., Kim, D.-H., 2016. 3D bioprinting for engineering complex tissues. *Biotech. Adv.* 34, 422–434.
- McCormack, A., Highley, C.B., Leslie, N.R., Melchels, F.P., 2020. 3D printing in suspension baths: keeping the promises of bioprinting afloat. *Trends Biotechnol.* 38, 584–593.
- Melchels, F.P., Domingos, M.A., Klein, T.J., Malda, J., Bartolo, P.J., Huttmacher, D.W., 2012. Additive manufacturing of tissues and organs. *Progr. Polym. Sci.* 37, 1079–1104.
- Miri, A.K., Hosseinabadi, H.G., Cecen, B., Hassan, S., Zhang, Y.S., 2018. Permeability mapping of gelatin methacryloyl hydrogels. *Acta Biomaterialia* 77, 38–47.
- Mironov, V., Boland, T., Trusk, T., Forgacs, G., Markwald, R.R., 2003. Organ printing: computer-aided jet-based 3d tissue engineering. *TRENDS Biotechnol.* 21, 157–161.
- Morrison, T.M., Choi, G., Zarins, C.K., Taylor, C.A., 2009. Circumferential and longitudinal cyclic strain of the human thoracic aorta: age-related changes. *J. Vascular Surgery* 49, 1029–1036.
- Mota, C., Camarero-Espinosa, S., Baker, M.B., Wieringa, P., Moroni, L., 2020. Bioprinting: from tissue and organ development to in vitro models. *Chem. Rev.* 120, 10547–10607.
- Narayanan, A., Rajan, A., Pramanik, R., Arockiarajan, A., 2019. A thermodynamically-consistent phenomenological viscoplastic model for hydrogels. *Mater. Res. Express* 6, 085418.
- Navara, A.M., Xu, Y., Perez, M.R., Mikos, A.G., 2023. Aspects of a suspended bioprinting system affect cell viability and support bath properties. *Tissue Eng.*
- Nikkhah, M., Eshak, N., Zorlutuna, P., Annabi, N., Castello, M., Kim, K., Dolatshahi-Pirouz, A., Edalat, F., Bae, H., Yang, Y., et al., 2012. Directed endothelial cell morphogenesis in micropatterned gelatin methacrylate hydrogels. *Biomaterials* 33, 9009–9018.
- Ning, L., Mehta, R., Cao, C., Theus, A., Tomov, M., Zhu, N., Weeks, E.R., Bauser-Heaton, H., Serpooshan, V., 2020. Embedded 3d bioprinting of gelatin methacryloyl-based constructs with highly tunable structural fidelity. *ACS Appl. Mater. Interfaces* 12, 44563–44577.
- Ouyang, L., Armstrong, J.P., Lin, Y., Wojciechowski, J.P., Lee-Reeves, C., Hachim, D., Zhou, K., Burdick, J.A., Stevens, M.M., 2020. Expanding and optimizing 3d bioprinting capabilities using complementary network bioinks. *Sci. Adv.* 6, eabc5529.
- Pahoff, S., Meinert, C., Bas, O., Nguyen, L., Klein, T.J., Huttmacher, D.W., 2019. Effect of gelatin source and photoinitiator type on chondrocyte redifferentiation in gelatin methacryloyl-based tissue-engineered cartilage constructs. *J. Mater. Chem. B* 7, 1761–1772.
- Pepelanova, I., Kruppa, K., Scheper, T., Lavrentieva, A., 2018. Gelatin-methacryloyl (gelma) hydrogels with defined degree of functionalization as a versatile toolkit for 3d cell culture and extrusion bioprinting. *Bioengineering* 5, 55.
- Piao, Y., You, H., Xu, T., Bei, H.-P., Piwko, I.Z., Kwan, Y.Y., Zhao, X., 2021. Biomedical applications of gelatin methacryloyl hydrogels. *Engineered Regeneration* 2, 47–56.
- Poldervaart, M.T., Gremmels, H., van Deventer, K., Fledderus, J.O., Öner, F.C., Verhaar, M.C., Dhert, W.J., Alblas, J., 2014. Prolonged presence of vegf promotes vascularization in 3d bioprinted scaffolds with defined architecture. *J. Controlled Release* 184, 58–66.
- Puech, P.-H., Bongrand, P., 2021. Mechanotransduction as a major driver of cell behaviour: Mechanisms, and relevance to cell organization and future research. *Open Biol.* 11, 210256.

- Rajabi, N., Rezaei, A., Kharaziha, M., Bakhsheshi-Rad, H.R., Luo, H., RamaKrishna, S., Berto, F., 2021. Recent advances on bioprinted gelatin methacrylate-based hydrogels for tissue repair. *Tissue Eng. A* 27, 679–702.
- Roche, C.D., Sharma, P., Ashton, A.W., Jackson, C., Xue, M., Gentile, C., 2021. Printability, durability, contractility and vascular network formation in 3d bioprinted cardiac endothelial cells using alginate–gelatin hydrogels. *Front. Bioeng. Biotechnol.* 9, 636257.
- Schwab, A., Levato, R., D'Este, M., Piluso, S., Eglin, D., Malda, J., 2020. Printability and shape fidelity of bioinks in 3d bioprinting. *Chem. Rev.* 120, 11028–11055.
- Shafraan, K., Jeans, C., Kemp, S.J., Murphy, K., 2020. Dr Barbara S. Neumann: clay scientist and industrial pioneer; creator of laponite®. *Clay Minerals* 55, 256–260.
- Sharifi, S., Sharifi, H., Akbari, A., Chodosh, J., 2021. Systematic optimization of visible light-induced crosslinking conditions of gelatin methacryloyl (gelma). *Sci. Rep.* 11, 23276.
- Shie, M.-Y., Lee, J.-J., Ho, C.-C., Yen, S.-Y., Ng, H.Y., Chen, Y.-W., 2020. Effects of gelatin methacrylate bio-ink concentration on mechano-physical properties and human dermal fibroblast behavior. *Polymers* 12, 1930.
- Sugerman, G.P., Kakaletsis, S., Thakkar, P., Chokshi, A., Parekh, S.H., Rausch, M.K., 2021. A whole blood thrombus mimic: constitutive behavior under simple shear. *J. Mech. Behav. Biomed. Mater.* 115, 104216.
- Sun, M., Sun, X., Wang, Z., Guo, S., Yu, G., Yang, H., 2018. Synthesis and properties of gelatin methacryloyl (gelma) hydrogels and their recent applications in load-bearing tissue. *Polymers* 10, 1290.
- Tang, M., Rich, J.N., Chen, S., 2021. Biomaterials and 3d bioprinting strategies to model glioblastoma and the blood–brain barrier. *Adv. Mater.* 33, 2004776.
- Teixeira, A.M., Martins, P., 2023. A review of bioengineering techniques applied to breast tissue: Mechanical properties, tissue engineering and finite element analysis. *Front. Bioeng. Biotechnol.* 11, 1161815.
- Tripathi, S., Mandal, S.S., Bauri, S., Maiti, P., 2023. 3D bioprinting and its innovative approach for biomedical applications. *MedComm* 4, e194.
- Wang, Y., Zeinali-Davarani, S., Zhang, Y., 2016. Arterial mechanics considering the structural and mechanical contributions of ecm constituents. *J. Biomech.* 49, 2358–2365.
- Wei, Z., Lei, M., Wang, Y., Xie, Y., Xie, X., Lan, D., Jia, Y., Liu, J., Ma, Y., Cheng, B., et al., 2023. Hydrogels with tunable mechanical plasticity regulate endothelial cell outgrowth in vasculogenesis and angiogenesis. *Nat. Commun.* 14, 8307.
- Wu, Y., Xiang, Y., Fang, J., Li, X., Lin, Z., Dai, G., Yin, J., Wei, P., Zhang, D., 2019. The influence of the stiffness of gelma substrate on the outgrowth of pc12 cells. *Biosci. Rep.* 39, BSR20181748.
- Xu, H., Liu, Q., Casillas, J., Mcanally, M., Mubtasim, N., Gollahon, L.S., Wu, D., Xu, C., 2022. Prediction of cell viability in dynamic optical projection stereolithography-based bioprinting using machine learning. *J. Intell. Manuf.* 1–11.
- Xu, L., Varkey, M., Jorgensen, A., Ju, J., Jin, Q., Park, J.H., Fu, Y., Zhang, G., Ke, D., Zhao, W., et al., 2020. Bioprinting small diameter blood vessel constructs with an endothelial and smooth muscle cell bilayer in a single step. *Biofabrication* 12, 045012.
- Xu, L., Zhang, Z., Jorgensen, A.M., Yang, Y., Jin, Q., Zhang, G., Cao, G., Fu, Y., Zhao, W., Ju, J., et al., 2023. Bioprinting a skin patch with dual-crosslinked gelatin (gelma) and silk fibroin (silma): An approach to accelerating cutaneous wound healing. *Mater. Today Bio* 18, 100550.
- Yeung, T., Georges, P.C., Flanagan, L.A., Marg, B., Ortiz, M., Funaki, M., Zahir, N., Ming, W., Weaver, V., Janmey, P.A., 2005. Effects of substrate stiffness on cell morphology, cytoskeletal structure, and adhesion. *Cell Motil. Cytoskeleton* 60, 24–34.
- Yin, J., Yan, M., Wang, Y., Fu, J., Suo, H., 2018. 3D bioprinting of low-concentration cell-laden gelatin methacrylate (gelma) bioinks with a two-step cross-linking strategy. *ACS Appl. Mater. Interfaces* 10, 6849–6857.
- Yin, H., Zhu, M., Wang, Y., Luo, L., Ye, Q., Lee, B.H., 2023. Physical properties and cellular responses of gelatin methacryloyl bulk hydrogels and highly ordered porous hydrogels. *Front. Soft Matter* 2, 1101680.
- Young, A.T., White, O.C., Daniele, M.A., 2020. Rheological properties of coordinated physical gelation and chemical crosslinking in gelatin methacryloyl (gelma) hydrogels. *Macromol. Biosci.* 20, 2000183.
- Yue, K., Trujillo-de Santiago, G., Alvarez, M.M., Tamayol, A., Annabi, N., Khademhosseini, A., 2015. Synthesis, properties, and biomedical applications of gelatin methacryloyl (gelma) hydrogels. *Biomaterials* 73, 254–271.
- Zamani, M., Cheng, Y.-H., Charbonier, F., Gupta, V.K., Mayer, A.T., Trevino, A.E., Quettermous, T., Chaudhuri, O., Cahan, P., Huang, N.F., 2022. Single-cell transcriptomic census of endothelial changes induced by matrix stiffness and the association with atherosclerosis. *Adv. Funct. Mater.* 32, 2203069.
- Zgeib, R., Wang, X., Zaeri, A., Zhang, F., Cao, K., Chang, R.C., 2023a. Development of a low-cost quad-extrusion 3d bioprinting system for multi-material tissue constructs. *Int. J. Bioprinting* 0159.
- Zgeib, R., Wang, X., Zaeri, A., Zhang, F., Cao, K., Chang, R., 2023b. Development of an open-source low-cost modular quad-extrusion 3d bioprinter. In: *Intl. Mfg. Sci. & Eng. Conf. V001T03A013*.
- Zhang, Z., Jin, Y., Yin, J., Xu, C., Xiong, R., Christensen, K., Ringeisen, B.R., Chrisey, D.B., Huang, Y., 2018. Evaluation of bioink printability for bioprinting applications. *Appl. Phys. Rev.* 5.
- Zheng, B., Breton, J.R., Patel, R.S., Bhatia, S.R., 2020. Microstructure, microrheology, and dynamics of laponite® and laponite®-poly (ethylene oxide) glasses and dispersions. *Rheol. Acta* 59, 387–397.
- Zhu, W., Ma, X., Gou, M., Mei, D., Zhang, K., Chen, S., 2016. 3D printing of functional biomaterials for tissue engineering. *Curr. Opin. Biotechnol.* 40, 103–112.
- Zhu, W., Qu, X., Zhu, J., Ma, X., Patel, S., Liu, J., Wang, P., Lai, C.S.E., Gou, M., Xu, Y., et al., 2017. Direct 3d bioprinting of prevascularized tissue constructs with complex microarchitecture. *Biomaterials* 124, 106–115.
- Zhu, M., Wang, Y., Ferracci, G., Zheng, J., Cho, N.-J., Lee, B.H., 2019. Gelatin methacryloyl and its hydrogels with an exceptional degree of controllability and batch-to-batch consistency. *Sci. Rep.* 9, 6863.